Higher-Order Hierarchical Legendre Basis Functions in Applications

Kim, Oleksiy S.; Jørgensen, Erik; Meincke, Peter; Breinbjerg, Olav

Published in:
The Fourth Swedish Conference on Computational Electromagnetics

Publication date:
2007

Document Version
Publisher's PDF, also known as Version of record

HIGHER-ORDER HIERARCHICAL LEGENDRE BASIS FUNCTIONS IN APPLICATIONS

Oleksiy S. Kim[(I)], Erik Jørgensen[(II)], Peter Meincke[(I)], and Olav Breinbjerg[(I)]

[(I)]Email: osk@oersted.dtu.dk
Ørsted•DTU, Section for ElectroScience, Technical University of Denmark
Ørsteds Plads, Building 348, DK-2800 Kgs. Lyngby, Denmark

[(II)]Email: ej@ticra.com
TICRA, Læderstræde 34, DK-1201 Copenhagen K, Denmark

The higher-order hierarchical Legendre basis functions have been developed for effective solution of integral equations with the method of moments. They are derived from orthogonal Legendre polynomials modified to enforce normal continuity between neighboring mesh elements, while preserving a high degree of orthogonality. The basis functions are well-suited for solution of complex electromagnetic problems involving multiple homogeneous or inhomogeneous dielectric regions, metallic surfaces, layered media, etc. This paper presents real-life complex antenna radiation problems modeled with electromagnetic simulation tools based on the higher-order hierarchical Legendre basis functions.

1 Introduction

The employment of higher-order basis functions is one of the ways to reduce computational and memory demands for solving complex electromagnetic problems with the Method of Moments (MoM). While fast integral equation solvers, such as the Multilevel Fast Multiple Method (MLFMM) or the Adaptive Integral Method (AIM) reduce the complexity of the solution keeping the number of unknowns unchanged, the higher-order basis functions allow the number of unknowns to be substantially reduced without compromising the resulting accuracy.

The higher-order hierarchical Legendre basis functions [1] inherit unique orthogonality properties from the polynomial they are based on. Due to these properties the continuity condition at the interface between metal and dielectric can be explicitly satisfied in the volume-surface integral equation formulation [2]. In the hybrid physical optics-MoM (PO-MoM) formulation it is possible to establish an explicit projection of PO currents onto the basis functions [3]. Moreover, these basis functions yield a well-conditioned MoM matrix. Comparisons made in [1] and [4] for the surface and volume integral equations, respectively, show that these basis functions provide much lower condition number than higher-order hierarchical basis functions based on the power series expansion [5].

The basis functions are well-suited for solution of complex electromagnetic problems involving multiple homogeneous or inhomogeneous dielectric regions, metallic surfaces, layered media, as well as all types of material junctions. The hierarchical property allows

the expansion order to be adapted to the electrical size of each element to achieve the required accuracy and minimize the number of unknowns.

The higher-order hierarchical Legendre basis functions are employed in an electromagnetic simulation tool developed at the Technical University of Denmark as well as in the commercial reflector analysis program GRASP [6]. Both tools employ a higher-order geometry modeling by means of curvilinear hexahedral and quadrilateral elements as well as preconditioned iterative equation solvers of the Krylov subspace kind. To allow accurate simulations of very large structures, the higher-order MoM has been hybridized with the PO and parallelized for execution on shared memory computer platforms.

This paper presents real-life complex antenna radiation problems simulated with the developed electromagnetic tools. The examples involve an L-band antenna segment of a Microwave Radiometer with Aperture Synthesis (MIRAS) for the SMOS (Soil Moisture and Ocean Salinity) ESA satellite, an airborne P-band ice sounding radar in the presence of the aircraft body, a grooved lens for the ALMA (Atacama Large Millimeter Array) telescope, and a ring focus dual reflector antenna.

2 MIRAS L-band Antenna Segment

The MIRAS instrument is a 2D synthetic aperture interferometric radiometer, which consists of three arms in "Y" form and a central supporting structure (hub). Each arm is comprised of three segments that are folded to the sides of the hub during launch. There are a number of LICEF (Light Cost Effective Front-end) units equally distributed over the three arms and the hub. Each LICEF is an L-band receiver (1404-1423 MHz) integrated with a four-probe patch antenna. Investigatory antenna measurements of these units assembled on the arms have been performed at the DTU-ESA Spherical Near-Field Antenna Test Facility. Some results of accompanying numerical simulations are presented here.

Figure 1 shows parts of the mesh of a LICEF antenna. Measured and computed radiation patterns at $f = 1413.0$ MHz for the antenna on a 600×600 mm ground plane are compared in Fig. 2. One can observe that the results are in a good agreement. The mesh utilized in the simulations comprises 209 quadrilateral and 5 wire elements, which results in 1300 unknowns.

Meshes of 8 individual LICEF antennas combined with a mesh of a segment are sketched in Fig. 3. The back surface of the segment is not modeled, since its influence on the forward radiation in the angle sector of interest ($\theta < \pm 35°$) is negligible. The size of the segment is $1514 \times 608 \times 100$ mm. 1566 quadrilateral elements are used in the mesh. Due to different element sizes the polynomial orders from 1 to 3 are employed in the solution, yielding 7070 unknowns in total. It is assumed that if vertical ports (V-polarization perpendicular to the segment) of an active antenna are excited, all vertical ports in other passive antennas are loaded, while the orthogonal ports are all open. The computed radiation pattern for the 4-th antenna excited at $f = 1413.0$ MHz is presented in Fig. 4 along with the corresponding measured results. It is seen that the results are in a very good agreement.

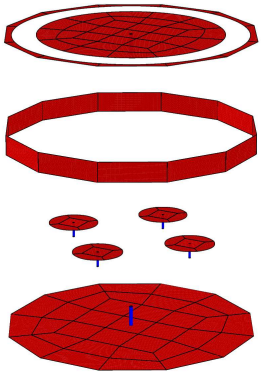

Figure 1: Mesh of a LICEF antenna.

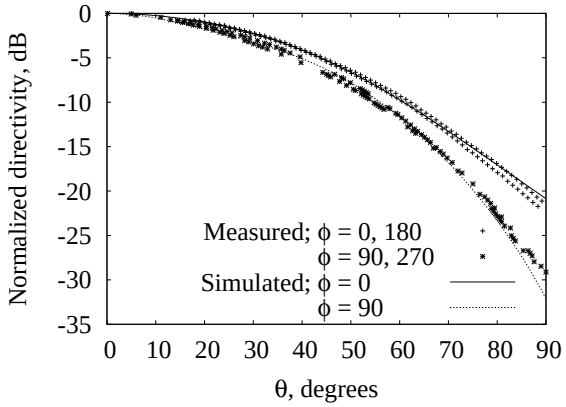

Figure 2: Measured and computed radiation patterns for a LICEF antenna on a 600 × 600 mm ground plane. $f = 1413.0$ MHz. Vertical polarization.

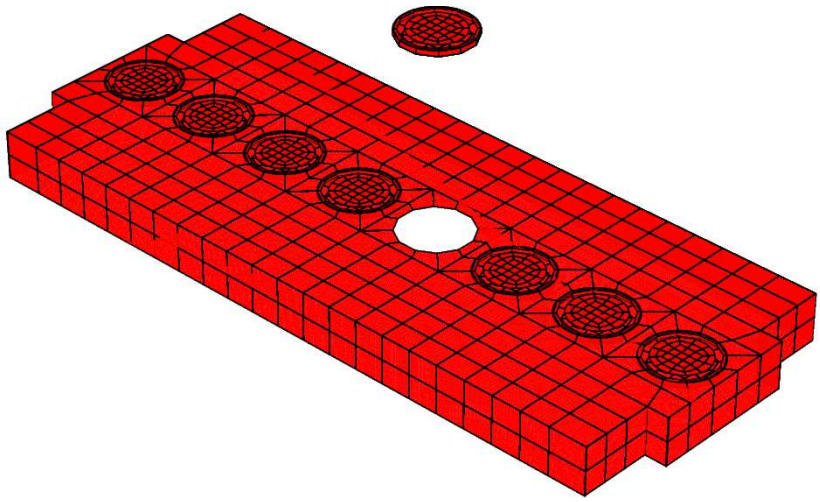

Figure 3: Mesh of an arm segment with 8 LICEF antennas.

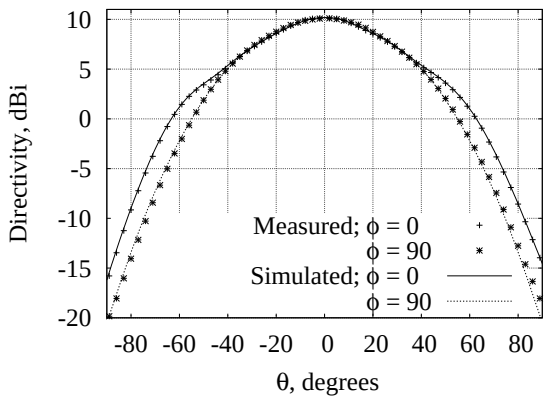

(a)

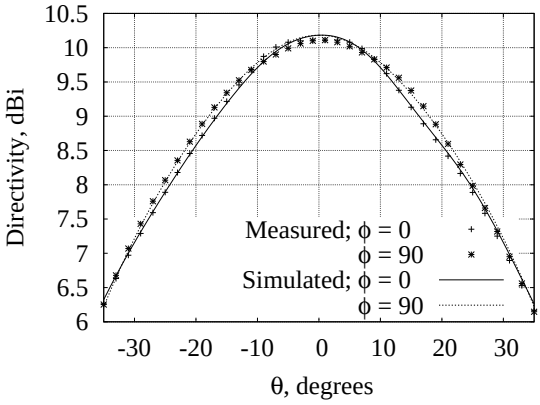

(b)

Figure 4: Measured and computed radiation patterns for the segment with the 4-th antenna excited at $f = 1413.0$ MHz. Plot (b) shows zoom-in of the plot (a).

3 P-band Ice Sounding Radar

The airborne P-band ice sounding radar is a demonstrator for the future ESA Earth Explorer mission. The radar employs an antenna array of 4 cavity-backed patches excited by a capacitive coupling to active small patches (Fig. 5). This dual polarized antenna array has been designed using an FDTD tool by CST Microwave Studio. However, the antenna characteristics are inevitably influenced by the massive metal aircraft body, which is supposed to carry the radar. This influence can hardly be investigated using FDTD, since the aircraft is too large to be included into the simulation domain. On the other hand, the higher-order MoM simulation tool can easily handle the problem.

The most important parts - the hull, the bottom sides of the wings, and the skies - that are expected to influence the radar most are included in the simulation (Fig. 6). The mesh including the antenna array employs 3138 flat and curved quadrilateral elements. At $f = 435.0$ MHz the simulation requires the polynomial orders from 1 to 3 and 19379 unknowns. Fig. 7 shows the computed radiation pattern of the antenna array in free space and on the aircraft.

4 Grooved Lens

The next example illustrates the ability to analyze a large dielectric object with sub-wavelength features. The object is a rotationally symmetric plano-convex teflon lens with circular grooves on both faces. This lens was designed for use in the ALMA telescope at 100 GHz and the cross-section of the grooved lens is shown in Fig. 8. The diameter of the lens is $10.0\lambda_0$, the groove depth is $0.21\lambda_0$, the groove width and the spacing between the grooves are $0.13\lambda_0$, and the relative permittivity is 2.158. The lens is mounted at the aperture of a corrugated horn.

The performance of the grooved lens was investigated using the higher-order MoM that has been integrated in the commercial program GRASP [6]. The corrugated feed horn was accurately analyzed by mode-matching [7] and the horn field was imported into GRASP as a spherical wave expansion. This expansion is only valid outside a sphere circumscribing the horn and cannot be used directly as excitation of the grooved lens which is mounted at the horn aperture. GRASP therefore converts the spherical wave expansion into a plane wave expansion which is valid in the half space $z > 0$ if the horn aperture is located in the plane defined by $z = 0$. The plane wave expansion can then be used to illuminate the lens.

The purpose of the grooves is to reduce the field reflected at the planar face of the lens. For a smooth lens without grooves, the power reflected at the planar face located at the horn aperture can be rather significant and cause a poor return loss of the horn-lens combination. To verify the design of the grooves, GRASP was used to compute the radiation patterns of the lens both with and without the grooves. The mesh of the smooth lens employs 348 4th-order quads which were approximately 2 by 2 wavelengths in the dielectric (see Fig. 9(a)). The large smooth patches calls for a high polynomial order and the maximum polynomial order used in this example is 8 resulting in 24320 unknowns. Despite the high polynomial order and the presence of dielectrics, the GMRES solution of the PMCHWT (Poggio-Miller-Chang-Harrington-Wu-Tsai Formulation) equations converges in 68 iterations due to the favorable orthogonality properties of the Legendre basis func-

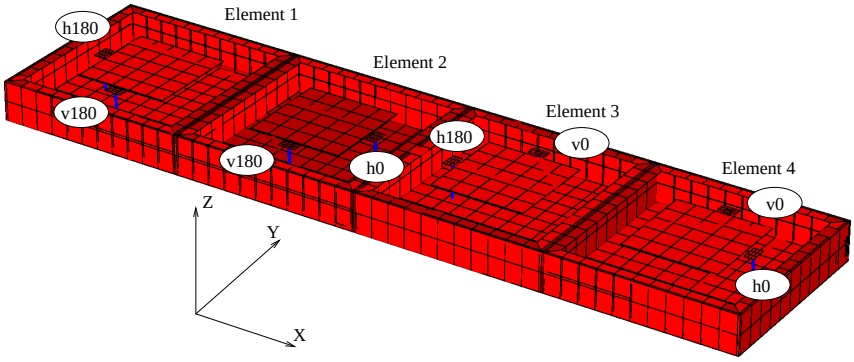

Figure 5: Mesh of the P-band radar antenna array.

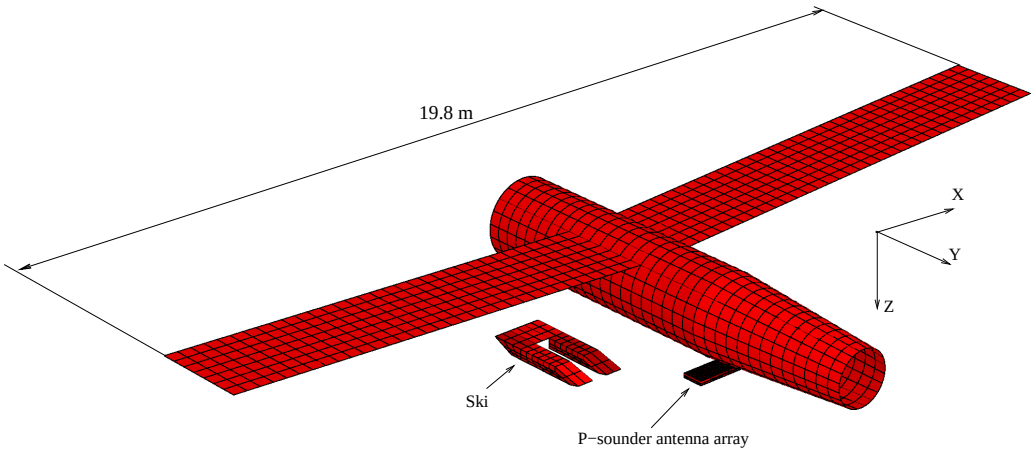

Figure 6: Mesh of the P-band radar antenna array. Phase of the excitation is shown for the vertical (v) and horizontal (h) polarizations.

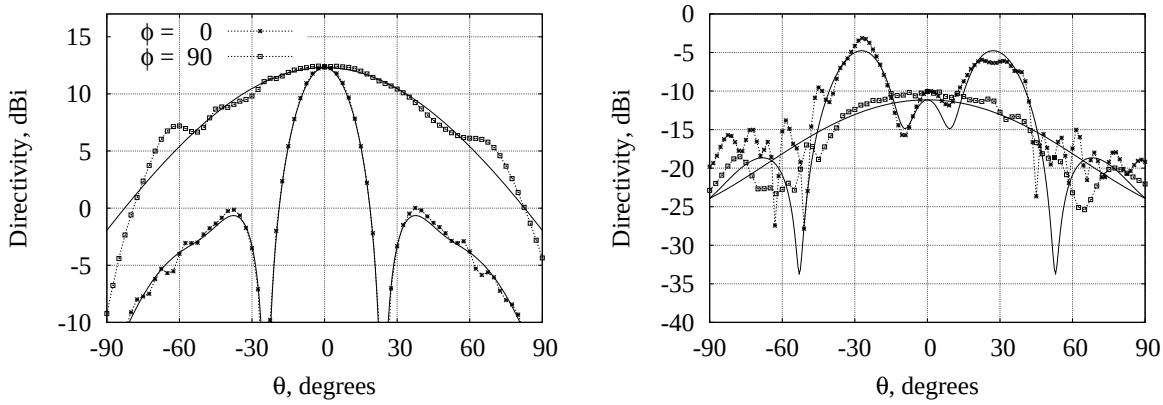

(a) (b)

Figure 7: Co- (a) and cross-polar (b) radiation pattern of the antenna array in free space (solid line) and on the aircraft (dotted line). All four elements are excited. Horizontal polarization. $f = 435.0$ MHz.

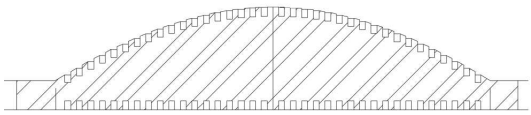

Figure 8: Cross-section of grooved plano-convex lens.

tions. The mesh of the grooved lens employs 2800 quads and is shown in Fig. 9(b). The length of the patch edges is anywhere between 0 and 2 wavelengths in the dielectric, and the majority of the patches are far from being square. The hierarchical expansion adapts to the size of each patch and employs different polynomial orders in each direction, e.g., 1 in the direction perpendicular to the grooves and 8 in the direction along the grooves. The total number of unknowns is 56320 and a direct solver is used.

Table 1 summarizes various parameters for the lens analysis. The power lost by reflection is reduced from 0.32 dB (7 percent) to almost nothing when the grooves are introduced. However, the peak co-pol increases 0.18 dB whereas the remaining power goes into the cross-pol and side lobes. This can be clearly seen in the polar radiation patterns of the horn-lens combination which are shown in Fig. 10. The smooth lens (dotted blue curve) yields a large co-polar back-lobe to the left in Fig. 10(a) but this lobe is dramatically reduced when the grooves are introduced (solid red curve). For the cross-pol in Fig. 10(b), the grooves also reduce the back-radiation but the peak in the front hemisphere is increased by 10.6 dB. Nevertheless, the grooved lens provides an excellent return loss and results in the best overall performance.

5 Ring Focus Dual Reflector Antenna

In this example, the importance of using higher-order geometry modeling is investigated by analyzing a ring focus reflector configuration shown in Fig. 11. The sub reflector has a sharp tip at the center which directs the rays away from the feed which can also be observed in the ray paths plotted in Fig. 11. However, the diameter of the sub reflector is only 5λ which makes the accuracy of the high-frequency methods in GRASP questionable, particularly due to the presence of the tip. With the higher-order MoM integrated in GRASP, the sub reflector can be accurately analyzed in a matter of seconds whereas the main reflector with a diameter of 40λ can be analyzed using the standard PO/PTD method in GRASP.

The radiation pattern of the sub reflector are obtained using 1st, 2nd, 3rd, and 4th order quads and the results are shown in Fig. 12. The mesh is the same in all four cases, except for the order of the patches. The curves for 3rd order patches (full line) and 4th order patches (crosses) are essentially the same, the curve for 2nd order patches deviates from the correct result, and the 1st order patches do not provide a usable accuracy. Based on this investigation, the built-in mesher in GRASP employs 3rd order patches by default. The execution time by going from 1st to 3rd order patches only increases 1-2 percent but this time is well spent due to the superior accuracy of the curved patches.

The radiation pattern of the ring focus antenna are shown in Fig. 13. The results have been obtained with two different methods: PO/PTD on both the sub reflector and the main reflector, and MoM on the sub reflector and PO/PTD on the main reflector. The result computed without MoM clearly shows that PO is not sufficiently accurate for analyzing the tip of the sub reflector. These results also includes the sub reflector blockage, i.e, the sub reflector is illuminated by both the horn and the currents on the main reflector. This implies that the MoM on the sub reflector is solved twice. The total execution time for obtaining the PO/PTD/MoM patterns in Fig. 13 was 20 seconds on a standard desktop PC.

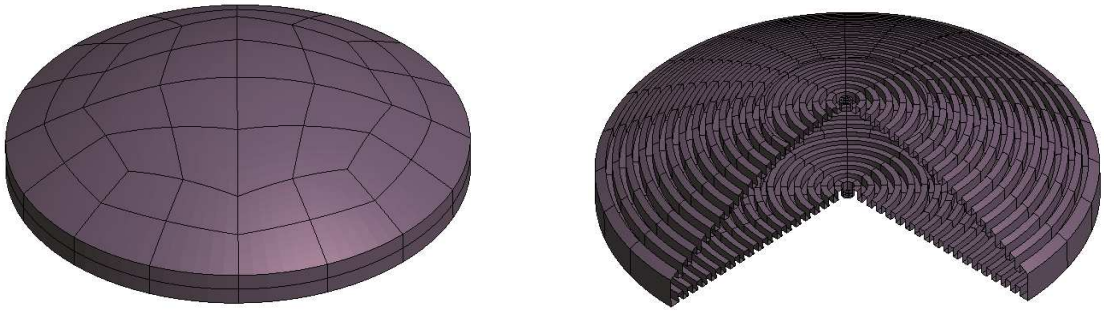

(a) (b)

Figure 9: Mesh of the smooth (a) and grooved (b) lens.

Table 1: Comparison of various parameters for the smooth and grooved lenses.

	Patches	Unknowns	Reflection	Peak co-pol	Peak cross-pol
Smooth	348	24320	0.32 dB	28.27 dB	-13.6 dB
Grooved	2800	56320	0.03 dB	28.45 dB	-3.0 dB

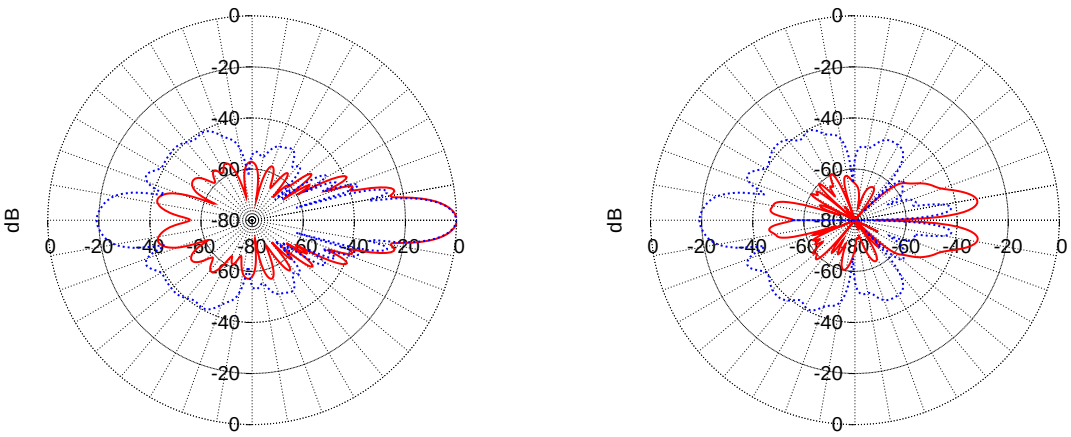

(a) (b)

Figure 10: Radiation pattern of the horn with the smooth (dotted blue curve) and the grooved (solid red) lens. The co-polar component is shown in (a) and the cross-polar in (b).

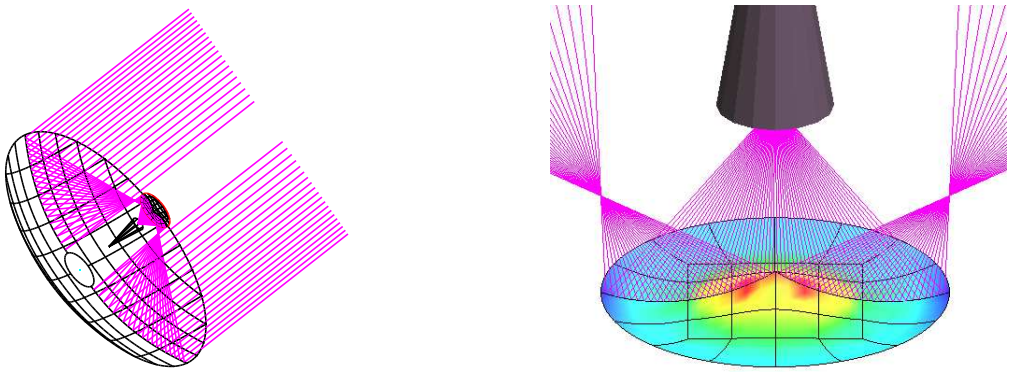

(a) (b)

Figure 11: Ring focus dual reflector antenna (a) and close-up of the feed and the sub reflector (b). The mesh (3rd order) of the sub reflector and the surface currents are also shown.

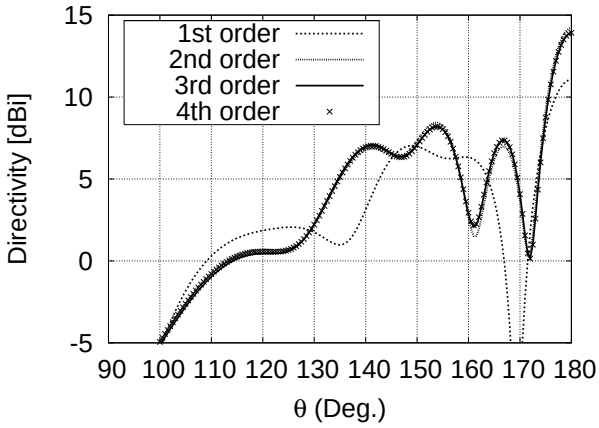

Figure 12: E-plane radiation pattern of horn and sub reflector (the direction $\theta = 180°$ is towards the main reflector). The results have been obtained using 1st, 2nd, 3rd, and 4th order patches in the mesh of the sub reflector.

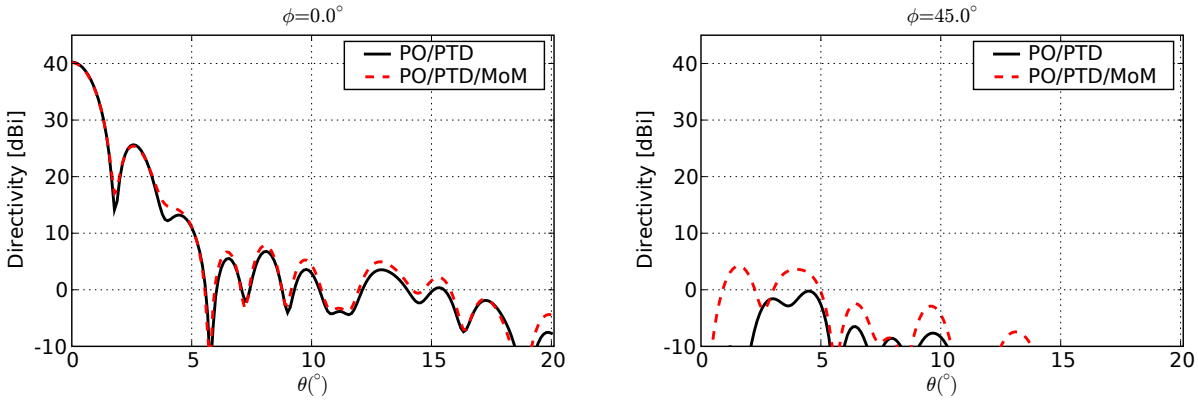

Figure 13: Radiation pattern of the ring focus antenna obtained with two different methods: PO/PTD on both reflectors (solid black curve) or PO/PTD on the main reflector and MoM on the subreflector (dashed red curve). Plots are shown for the co-polar component in the E-plane (left) and the cross-polar component in the $\phi = 45°$ plane (right).

References

[1] E. Jørgensen, J. L. Volakis, P. Meincke, and O. Breinbjerg. *IEEE Trans. on Antennas and Propagation*, 52(11):2985–2995, November 2004.

[2] O. S. Kim, P. Meincke, O. Breinbjerg, and E. Jørgensen. *Radio Science*, 42, RS4023, doi:10.1029/2006RS003584, 2007.

[3] E. Jørgensen, P. Meincke, and O. Breinbjerg. In *Proc. of the 2003 IEEE Antennas and Propagation Soc. Int. Symp.*, vol. 4, pp. 98–101, Columbus, OH, USA, 2003.

[4] O. S. Kim, P. Meincke, O. Breinbjerg, and E. Jørgensen. *Radio Science*, 39, RS5003, doi:10.1029/2004RS003041, 2004.

[5] B. M. Kolundžija and B. D. Popović. *IEE Proceedings-H*, 140(1):1–10, February 1993.

[6] TICRA, Copenhagen, Denmark, http://www.ticra.com, GRASP, General Reflector Analysis Program v. 9.3.03, 2007.

[7] TICRA, Copenhagen, Denmark, http://www.ticra.com, CHAMP, Corrugated horn analysis by modal processing, 2007.